Research article

Evaluation of photoassisted treatments for norfloxacin removal in water using mesoporous Fe$_2$O$_3$-TiO$_2$ materials

Patricia García-Muñoz[a,b,*], Niels P. Zussblatt[b], Gema Pliego[a], Juan A. Zazo[a], Fernando Fresno[c], Bradley F. Chmelka[b], Jose A. Casas[a]

[a] Departamento de Ingeniería Química, Facultad de Ciencias, Universidad Autónoma de Madrid, 28049, Madrid, Spain
[b] Department of Chemical Engineering, University of California, Santa Barbara, CA, 93106, United States
[c] Photoactivated Processes Unit, IMDEA Energy Institute, Móstoles, 28935, Madrid, Spain

ABSTRACT

We report the synthesis of mesoporous TiO$_2$ and mesoporous Fe$_2$O$_3$-TiO$_2$ catalysts by using a structure-directing-surfactant method, their characterization and their employment as photocatalysts for norfloxacin degradation in aqueous solution. The main findings show that in the presence of both O$_2$ and H$_2$O$_2$, Fe-containing mesoporous titania (Fe$_2$O$_3$-TiO$_2$), with iron percentages between 1 and 3 wt%, exhibited norfloxacin degradation rates more than 60% greater than otherwise identical mesoporous titania without iron. Furthermore, the activity of the mesoporous composite catalysts also exceeds that of titania when illuminated with 405 nm light-emitting diodes. Iron loading improved the photocatalytic activity for norfloxacin degradation with values of apparent reaction rate constants of 0.037 min^{-1} and 0.076 min^{-1} with 1 and 3 surface wt.% of iron, respectively. An optimum of activity was found with the 3 wt% Fe$_2$O$_3$-TiO$_2$ catalyst. Under these conditions, 10 mg/L of norfloxacin is reacted essentially to completion and 90% of total organic carbon conversion was obtained within 120 min of reaction. This higher organic carbon conversion degree was reached due to the photo-oxidation of short-chain organic acids. The high activity of the as-synthesized mesoporous composites is attributed to the additional iron phase which led to the different reactions for H$_2$O$_2$ decomposition, but also due to the improvement in light absorbance. Finally, the activity of the most active catalyst was found to be stable over multiple sequential runs, which was related to a negligible amount of iron leaching ($< 0.1\%$) from these materials.

1. Introduction

The occurrence of pharmaceuticals and their metabolites in the environment is becoming of increased concern, as the presence of these substances can provoke adverse effects on living organisms, increase bacterial resistance to antibiotics, or result in ecological risks such as the reduction of phytoplankton populations (Dinh et al., 2017; Baquero et al., 2008; Emmanuel et al., 2005). For these reasons, in 2015 the European Union produced the first list of substances to be monitored in its Decision *2015/498/EU* (Barbosa et al., 2016). This list includes ten new groups of substances that must be controlled, including pharmaceutical products (Barbosa et al., 2016). Among the listed pharmaceuticals, special importance has been given to antibiotics, because of the known development of antibiotic-resistant bacteria. Extensive use of antibiotics has resulted in their presence in wastewater at concentrations ranging from ng·L^{-1} to μg·L^{-1} (Verlicchi et al., 2012). Conventional wastewater treatment plants (WWTPs) are not able to completely degrade these compounds, resulting in their release to natural water bodies (Hughes et al., 2013). To address this deficiency in current water treatment practices, research is moving towards non-conventional treatments such as Advanced Oxidation Processes (AOPs), based on the generation of hydroxyl radicals (HO·) to attack non-biodegradable organic matter. This radical is both very reactive and non-selective.

Fluoroquinolones are the third largest group of antibiotics accounting for 17% of the global market share (Van Doorslaer et al., 2014). Norfloxacin (NOR) belongs to this family and presents a vast range of antibacterial activity, being one of the most widely used antibiotics for human and veterinary purposes and one of the most relevant second-class synthetic antibiotics. NOR and its metabolites can appear in their active forms in natural water bodies, because they are not completely eliminated in WWTPs. It has been detected in a wide range of concentrations in several parts of the World. While in water of the Atlantic and the Antarctic oceans it has been detected in concentrations around 95 ng/L and 0.8 μg/L (He et al., 2019; Hernández

et al., 2019), in some municipal wastewater in Europe and China the measured concentrations exceeded the values of 200 ng/L (Wang et al., 2019; Paíga et al., 2019). For this reason, there are several studies dealing with AOPs for the treatment of fluoroquinolones (Kanakaraju et al., 2018). For instance, chlorination was studied by Dodd et al. (2005), which showed that some fluoroquinolones were recalcitrant to the process, generating halogenated intermediates. Jiang and co-workers (Jiang et al., 2016) employed sulfate radical oxidation, finding that after 3 h at 60 °C, complete antibiotic removal was achieved, but at the end of the process, the water contained significant concentrations of salt that needed to be removed prior to discharge. The ozonation under UV of a preconcentrated effluent was also investigated by Liu et al. (2014), leading to 87% of antibiotic removal and a COD reduction of 40%. Nevertheless, in most cases, incomplete total organic carbon conversion of the bactericidal active compound renders processes unsuitable or requires additional post-treatment stages.

Photocatalytic processes using titania (TiO₂) catalysts have been proven to be an effective complementary treatment to WWTPs and in some cases even an alternative (Malato et al., 2009) for the treatment of pharmaceutical wastes (Sarkar et al., 2015; Rey et al., 2014; García-Muñoz et al., 2017a; Chakraborty et al., 2017; Kanakaraju et al., 2016). In general, a photocatalytic process consists of the excitation of a semiconductor when it absorbs incident light of enough energy to generate electron-hole pairs. Such pairs subsequently generate free radicals (e.g., hydroxyl radicals, HO·) that undergo secondary reactions with contaminants that lead to their degradation and in the most favorable cases to their complete mineralization. In this sense, diverse radiation sources featuring either broad UV–visible light spectra or discrete wavelengths can be employed. The recent development and use of solid-state light-emitting diode (LED) sources with a single emission wavelength presents several advantages, among which higher current-to-light conversion efficiencies, lower heating, narrow band emission, and long life stand out (Pliego et al., 2016; Korovin et al., 2015). However, LED emission wavelengths must match the maximum absorption range of the catalyst to be most effective.

Titania is a widely used photocatalyst because of its resistance to corrosion, high activity, and low toxicity as has been recently corroborated (Bohdziewicz et al., 2016). It is also a good candidate to be modified for being active under monochromatic light from a UVA-LED. A possible transition metal to include onto titania surfaces is iron, which has a relatively high abundance on Earth, is non-toxic and can alter the light absorption towards the visible region (Litter and Navío, 1996; Měšťánková et al., 2005; Tryba et al., 2006; Yalçın et al., 2010). Fe₂O₃ is a n-type semiconductor but its low band-gap value (with a fast recombination of charges) and the positions of the conduction and valence bands make it individually an unsuitable photocatalyst for oxidation reactions. Nevertheless, a composite catalyst which incorporates both iron and titanium oxides seems a good alternative to promote the separation of photogenerated charges and to reduce their recombination (Fresno, 2013). In addition, the Fe(II)/Fe(III) redox cycle in presence of H₂O₂ can substantially improve the rates of oxidation processes due to the generation of additional oxidative radicals through the Catalytic Wet Peroxide Oxidation (CWPO) process (Tryba et al., 2006). Briefly, this process is based on the generation of hydroxyl radicals by decomposing H₂O₂ in presence of a metallic salt or phase, e.g. iron salts or iron oxide. Recently, Shao et al. (2017) combined α-Fe₂O₃/H₂O₂ under visible irradiation to enhance the degradation rates of organic pollutants in water with an enhanced efficiency of the process. Also, Garcia-Muñoz et al. (García-Muñoz et al., 2016, 2017a, 2018) employed FeTiO₃ natural catalyst in presence of H₂O₂ and light to remove organic pollutants and specifically sulfonamides antibiotics for water.

There exist many prior studies that have examined the catalytic potentials of modified mesoporous TiO₂ materials. These materials are expected to provide facile diffusion of large organic molecules to internal active sites, compared to catalysts with sub-nanometer pores (so-called microporous). These studies also showed that mesoporosity enhances the light harvesting as a result of the light reflections inside the framework and also improves the photoactivity due to the existence of alternate transfer pathways of charge carriers. For instance, Zhou et al. (Yu et al., 2018) synthesized a mesoporous C₃N₄-TiO₂ composite and tested it for sulfamethoxazole removal in water. Kundu et al. (2017) incorporated silver onto mesoporous titania for rhodamine B removal. Recently, Ismail et al. (2018) reported the use of a gallium oxide over a titania catalyst for herbicide depletion in water. However, to the best of the authors' knowledge, no prior studies have involved the use of highly porous Fe₂O₃-TiO₂ catalysts for the removal of the non-biodegradable norfloxacin antibiotic from water. In this sense, the combination of iron and titanium oxides can solve some drawbacks of single AOPs by taking advantage of both CWPO and photocatalysis processes.

The aim of this work is the synthesis, characterization and testing of mesoporous Fe₂O₃-TiO₂ catalysts for the photocatalytic removal of norfloxacin in water through the implementation of a combined photocatalytic H₂O₂-assisted process with a unique catalyst. The influence of O₂ and H₂O₂ as oxidizing agents and of different radiation sources on the degradation of NOR have been evaluated, along with the dependence on iron content to gain insight into its role in a possible photocatalytic degradation mechanism. In addition, the stabilities of catalysts were evaluated in terms of loss of active phase and reusability in sequential runs.

2. Materials and methods

2.1. Syntheses of mesoporous titania materials

Mesoporous titania materials were prepared by a method involving the calcination of a composite cross-linked titania and structure-directing-surfactant material (Yang et al., 1999). The titania-surfactant composite was prepared by drying a mixture of titanium tetrachloride, ethanol, and a triblock-copolymer surfactant, $HO(CH_2CH_2O)_{106}(CH_2CH(CH_3)O)_{70}(CH_2CH_2O)_{106}H$ (Pluronic™ F127). In a typical synthesis, 1 g of the Pluronic™ F127 triblock-copolymer (Sigma-Aldrich) was dissolved in 10 g of anhydrous ethanol. Following complete dissolution of the triblock copolymer, 1.90 g of $TiCl_4$ (Acros, 99.9% purity) was added dropwise with vigorous stirring. The mixture was then poured into a Petri dish and dried for 7 days at 40 °C to yield the titania-surfactant composite. Once drying was complete, the titania-surfactant composite films were placed in a ceramic crucible for calcination, which was carried out under air at 400 °C for 5 h with heating and cooling ramp rates of 1 °C min⁻¹, resulting in removal of the structure-directing surfactant species and formation of a mesoporous titania powder.

Iron-grafted mesoporous titania was prepared by adding 1 g of mesoporous titania powder and various quantities (80, 160, 320, or 640 mg) of anhydrous $FeCl_3$ into 50 mL of anhydrous ethanol. This mixture was stirred for 6 h, and after vacuum filtering, which resulted in tan powders that were subsequently dried at 90 °C for 6 h.

2.2. Materials characterization

Nitrogen sorption isotherms were acquired at 77 K with MicroMeritics Tristar 3000 equipment, and samples were dried overnight at 120 °C under flowing N₂ before the measurements. The surface areas were calculated by using the Brunauer-Emmett-Teller (BET) method, while pore volumes and size distributions were calculated by using the Barrett-Joyner-Halenda (BJH) method. X-ray diffraction (XRD) patterns were recorded in a Panalytical EMPYREAN diffractometer using CuK$_\alpha$ radiation (λ = 1.54178 Å) with a rate of 0.01 °s⁻¹ and a step size of 0.013°. The iron and titanium content of materials was determined by total reflection X-ray fluorescence (TXRF), using a TXRF spectrometer 8030c.

Surface composition was characterized to 0.1 atom% accuracy by X-ray photoelectron spectroscopy (XPS) using a Kratos Axis Ultra X-ray

photoelectron spectroscopy system. Surface elemental compositions were determined by averaging three survey scans over a range of 0–800 eV with a step size of 0.25 eV and a pass energy of 160 eV. Spectra were processed using Casa XPS software, and were referenced by setting the position of the adventitious carbon C 1*s* peak to 284.6 eV (Shard, 2014). Surface atomic compositions were used to calculate surface mass compositions. Scanning electron microscopy (SEM) was conducted on a Hitachi TM 1000 instrument with an energy dispersive X-ray analyzer.

2.3. Photoactivity runs

Two different sets of reactions were performed employing different reactor configurations (Supplementary Material, Fig. S1). The first set was carried out in an immersion-wall batch photoreactor with a 150 W medium pressure Hg lamp (TQ-150, Heraeus) contained in a water-cooled quartz double-walled jacket. The lamp emitted in a 200–600 nm spectra. The UV irradiance was 30 W m^{-2} measured by a photo-radiometer (Photo-radiometer Delta Ohm HD 2102.1). The reaction volume was 700 mL. The catalyst concentration was optimized (500 mg L^{-1}). A second set of reactions was performed in a counter-flow quartz concentric tubular reactor (100 mL useful volume). The aqueous solution (norfloxacin, Fluka > 98%) and the catalyst coursed through the intermediate wall. Both were continuously recirculated (with a peristaltic pump) to maintain the catalyst suspended. A commercial LED strip (SMD 5050) was placed around the external wall of the reactor. The irradiance corresponding to 405 nm LED radiation was 10 W m^{-2}. In these experiments, catalyst optimum concentration was 50 mg L^{-1}.

Two different oxidants were tested. Pure oxygen (Praxair, 99.5%) (10 mL min^{-1}) was used in the photocatalytic trials and H$_2$O$_2$ (Panreac 33% v/v), for the CWPO-photoassisted process, with a dose corresponding to the stoichiometric amount for complete mineralization of norfloxacin (26 mg L^{-1}).

All of the experiments were carried out by triplicate at 278 K, an initial pH$_0$ of 7 (natural pH of norfloxacin solution) and 10 mg L^{-1} of initial aqueous norfloxacin solution. To compare with the synthesized materials, reactions with the reference AEROXIDE TiO$_2$ P25 catalyst (Evonik, 80% anatase – 20% rutile) were also carried out.

2.4. Analytical methods

Norfloxacin concentrations were measured by high-performance liquid chromatography (HPLC) using a Varian Pro-Star 240 with a diode array detector (330 PDA). A Microsorb C18 5 μm column (MV 100, 15 cm long, 4.6 mm diameter) was used as stationary phase and 1 mL min^{-1} of 4 mM aqueous sulfuric solution and acetonitrile (75:25) was used as mobile phase. Short-chain organic acids were analyzed by an ion chromatograph (Metrohm 790 IC) using a conductivity detector. A Metrosep A supp 5–250 column (25 cm length, 4 mm diameter) was employed as stationary phase, while an aqueous solution containing 3.2 mM Na$_2$CO$_3$ and 1 mM NaHCO$_3$ was employed as mobile phase at a flowrate of 0.7 mL min^{-1}. Total organic carbon (TOC) was determined using a TOC analyzer (Shimadzu, model 5000 A). Hydrogen peroxide was determined by colorimetric titration using the TiOSO$_4$ method (Eisenberg, 1943). Finally, leached iron was quantified by ortho-phenanthroline method (Sandell, 1945).

3. Results and discussion

3.1. Materials characterization

Table 1 shows the main chemical, structural and textural characteristics of the obtained catalysts, together with those of P25 for comparison. The surface Fe/Ti ratio, determined by XPS, increased with the iron content of the catalysts, as shown in Table 1, which resulted

Table 1
Properties of standard and synthesized materials.

Catalyst	Phases	S$_{BET}$ (m^2/g)	Pore width (A)	XPS(% w/w)		TXRF (% w/w)	
				Ti	Fe	Ti	Fe
P25 reference	A/R	50	n. m.	n.m.	n.m.	n.m.	n.m.
TiO$_2$	A	178	100	59.9	0.0	57.8	0.0
Fe$_2$O$_3$ (1.0)-TiO$_2$	A	172	95	59.6	1.0	57.5	0.05
Fe$_2$O$_3$ (1.5)-TiO$_2$	A	165	97	58.8	1.5	57.8	0.08
Fe$_2$O$_3$ (2.1)-TiO$_2$	A	158	100	58.1	2.1	57.8	0.12
Fe$_2$O$_3$ (3.0)-TiO$_2$	A	150	99	57.5	3.0	57.9	0.18

A: anatase; R: rutile; n.m.: not measured.

from the different amounts of FeCl$_3$ used in their syntheses. The different catalysts were named Fe$_2$O$_3$(1.0)-, Fe$_2$O$_3$(1.5)-, Fe$_2$O$_3$(2.1)- and Fe$_2$O$_3$(3.0)-TiO$_2$ according to their surface iron contents of 1.0, 1.5, 2.1 and 3.0 wt%, respectively. The bulk iron contents, determined from TXRF spectra, are considerably lower than those obtained from XPS, indicating that iron is mostly present in the surface of the materials, as expected from the synthesis method. The Fe2p regions of the XPS spectra (Supplementary Material, Fig. S2) show in all cases photo-emission peaks in good agreement with those expected for Fe(III) in Fe$_2$O$_3$ (Carraro et al., 2013).

The wide-angle X-ray diffraction pattern (Supplementary Material, Fig. S3) of mesoporous TiO$_2$ shows reflections indexable to the anatase phase by comparison with the ICDD PDF no. 21–1272. The iron-containing materials show essentially identical XRD patterns to that of the Fe-free TiO$_2$. Thus, no new reflections attributable to iron phases are observed even in the sample with the highest iron oxide loading, which is consistent with the low bulk iron contents shown in Table 1 and indicating the absence of significant crystalline iron oxide. In addition, no displacement of the reflections occurs with the presence of iron, suggesting that Fe-doping of TiO$_2$ does not occur, as expected from the soft synthesis method and in accordance with the XPS observations. Similarly, all samples present similar anatase crystal sizes (between 12.2 and 12.5 nm from the Scherrer equation) regardless of the iron content. In nitrogen sorption, all the catalysts show a type-IV isotherm typical of mesoporous materials (Fig. 1A), from which the BET surface area of TiO$_2$ was determined to be 178 m^2 g^{-1}, which gradually decreases with increasing iron loading down to 150 m^2 g^{-1} with the highest iron content (Table 1), probably because iron oxide is anchored inside the pores (Ismail et al., 2018). Also, the hysteresis loop indicates the loss in long-range ordering of the mesopores when the iron phase is included (Fig. 1A) (Yang et al., 1999). The pore size distribution for all cases is centred around 10 nm, corroborating the mesoporosity (Fig. 1B and Table 1).

Thermogravimetric analyses indicated that the triblock copolymer structure-directing species were completely removed upon calcination in air at 400 °C (Supplementary information, Fig. S4). The absence of a mass gain at high temperatures also suggests the absence of Fe(II) species that would oxidize and uptake oxygen during TGA. Concerning the electronic properties, diffuse reflectance UV–visible spectra (Fig. 2) show the absorption onset of mesoporous TiO$_2$ at ca. 405 nm, typical of the anatase phase (Fresno et al., 2008). By comparison, the mesoporous Fe$_2$O$_3$-TiO$_2$ materials show an additional absorption in part of the visible region (400–600 nm), that increases in intensity with increasing iron loading, consistent with the presence of Fe$_2$O$_3$ (Zhu et al., 2006) and with the changes in catalyst colour from white for pure TiO$_2$ to light yellow for the samples containing iron. SEM images (Supplementary material, Fig. S5) show in all cases agglomerates of different sizes regardless of the presence and content of Fe$_2$O$_3$. The texture of the larger particles in higher magnification images suggests that they are indeed agglomerates of smaller ones. EDX analysis showed the presence of iron in all the analyzed areas of the Fe$_2$O$_3$-loaded samples regardless of the size of the target agglomerate.
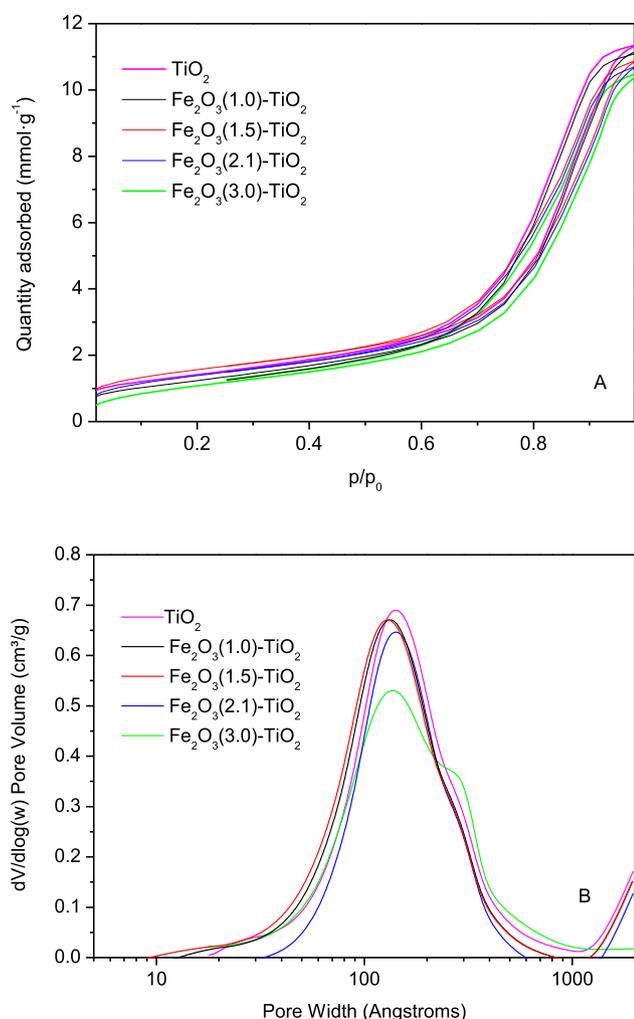
Fig. 1. (A) N_2 adsorption-desorption isotherms at 77 K and (B) BJH pore size distributions of mesoporous catalysts.
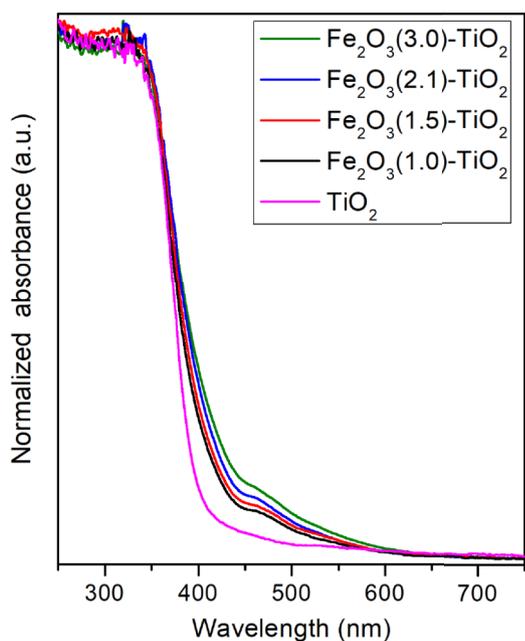
Fig. 2. Diffuse reflectance UV–vis spectra of mesoporous TiO_2 and mesoporous Fe_2O_3-TiO_2.
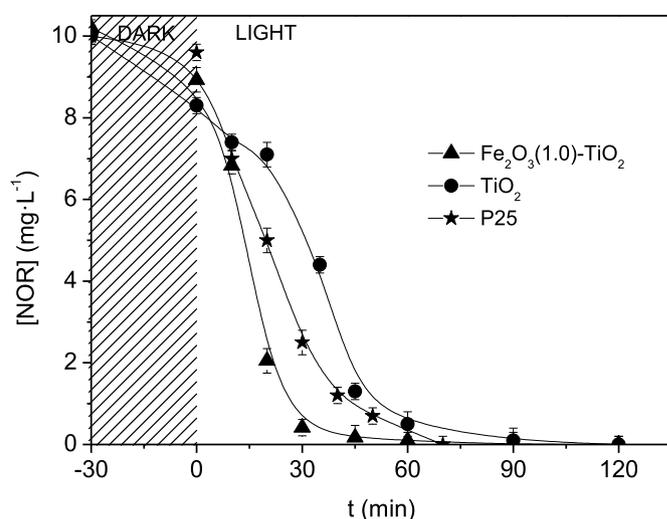
Fig. 3. Transient concentrations of norfloxacin in aqueous solution during photo-oxidation at 298 K and pH 7 in the presence of P25, mesoporous TiO_2, and mesoporous $Fe_2O_3(1.0)$-TiO_2 catalysts and under UV light illumination by a Hg lamp. (Operating conditions: $[NOR] = 10\,mg\,L^{-1}$; $[O_2] = 10\,mL\,min^{-1}$; $\lambda = 200–600\,nm$; $V_R = 0.7\,L$).

3.2. Photocatalytic activity

Mesoporous TiO_2 and mesoporous Fe-containing TiO_2 materials were employed as photocatalysts for NOR degradation using O_2 as oxidizing agent. Fig. 3 depicts NOR evolution during the reactions with mesoporous TiO_2, P25 titania and mesoporous $Fe_2O_3(1.0)$-TiO_2 catalysts. The synthesized materials showed different behaviour compared to the P25 reference catalyst.

Initially, a dark period was carried out for 30 min, the time required to reach the adsorption/desorption equilibrium as was observed in adsorption experiments (Fig. S6). When P25 was employed, a negligible adsorption of NOR onto its surface was seen. Nevertheless, mesoporous TiO_2 and mesoporous $Fe_2O_3(1.0)$-TiO_2 showed a remarkably high adsorption related to the presence of mesopores. The adsorption amounts were 20% of the initial charge for TiO_2 and $\approx 12\%$ for the Fe_2O_3-loaded material, which is in line with the anchorage of iron phase onto the external surface provoking a slight reduction of the surface area.

Once adsorption equilibrium was reached, a photo-oxidative stage under irradiation took place, leading to a complete NOR depletion by all three materials (Fig. 3). The degradation curve using mesoporous TiO_2 was similar to the one obtained with the P25 commercial reference catalyst, which confirmed the photoactivity of the former material. However, the presence of an induction period before NOR removal at 90 min was noticeable. This fact could be related to the high adsorption capacity of this material. In the case of P25, NOR oxidation started at the onset of irradiation and achieved complete depletion in 70 min. A typical photocatalysis mechanism is proposed (Eqs. (1)–(4)) where a photoactive phase generates charges which react with acceptor and donor species. The fact that NOR was adsorbed implies an easy reaction with surface generated radicals.

$$TiO_2 \xrightarrow{h\nu} e^- + h^+ \tag{1}$$

$$e^- + O_2 \rightarrow O_2^{\cdot -} \xrightarrow{H^+} HOO\cdot \tag{2}$$

$$h^+ + H_2O \rightarrow HO\cdot + H^+ \tag{3}$$

$$NOR + HOx\cdot \rightarrow oxidized\ intermediates \tag{4}$$

Notably, the introduction of iron onto the mesoporous TiO_2 catalyst improved the photocatalytic processes (Fig. 3) and overcame some drawbacks of TiO_2 alone. The results indicated that the photo-

degradation rate associated with the Fe₂O₃ (1.0)-TiO₂ catalyst was almost two times greater than with pristine mesoporous TiO₂. In photocatalysis, this enhancement is mainly derived from the presence of another photoactive phase (Fe₂O₃) with a low band-gap value and indicates contributions of visible light activation to the reaction. The additional number of acceptors from the iron species promotes the formation of electron-hole pairs, reducing the recombination of charges (Liu et al., 2018; Luan et al., 2014). As a result, complete degradation of the NOR antibiotic occurred in a shorter period (60 min) after the onset of irradiation. The reaction scheme is more complex in the presence of iron. On the one hand, the presence of iron promotes the charge mobility between Fe₂O₃ and TiO₂ and is expected to speed electron transfer (Lee et al., 2017; Moniz et al., 2014). On the other hand, the presence of light contributes to faster iron regeneration by closing the Fe(III)/Fe(II) redox cycle (Pliego et al., 2016; García-Muñoz et al., 2016, 2017b; Zazo et al., 2016) and improving the photo-efficiency. The absence of induction period in the presence of iron confirms the large generation of oxidizing species.

To gain further information about the degree of mineralization, the concentration of oxidation intermediates, specifically short-chain acids (mainly oxalic, acetic and formic), were measured. Larger amounts of short-chain acids species detected in the case of mesoporous TiO₂ at the end of reaction (Table 2) indicated the scarce total organic carbon (TOC) conversion of the antibiotic compound compared to those concentrations detected for Fe₂O₃(1.0)-TiO₂ catalyst. In the presence of Fe₂O₃-TiO₂, the lower acids amounts can be associated to their complete oxidation to CO₂.

The activity of the three catalysts increased using H₂O₂ as oxidant, and under these conditions mesoporous TiO₂, P25, and mesoporous Fe₂O₃(1.0)-TiO₂ achieved essentially complete NOR degradation in 60, 50 and 30 min of reaction, respectively (Fig. 4). This high photoactivity was related to the hydrogen peroxide decomposition into oxidizing radicals (right axis in Fig. 4). The induction period observed for mesoporous TiO₂ with O₂ was not observed in this case, and the antibiotic was degraded after 60 min, even though H₂O₂ was not completely depleted. The increased generation of radicals caused by the additional reactions (Eqs. (5) and (6)) promoted faster antibiotic decomposition. Hydrogen peroxide acted as an acceptor of both electrons and holes, generating radicals that oxidized organic molecules (Eq. (7)) and reducing charge recombination as well.

$$H_2O_2 + h^+ \rightarrow + HOO\cdot + H^+ \tag{5}$$

$$H_2O_2 + e^- \rightarrow + HO\cdot + OH^- \tag{6}$$

$$NOR + HO\cdot_x \rightarrow oxidized\ intermediates \tag{7}$$
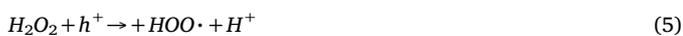
However, in addition to the reactions mentioned above, when H₂O₂ was used with the iron-containing mesoporous Fe₂O₃-TiO₂ catalyst, those pertinent to *Catalytic Wet Peroxide Oxidation* (CWPO, or heterogeneous Fenton) were of greater importance. These reactions included iron oxidation-reduction in the presence of H₂O₂ to generate HO_x which constituted another contribution to NOR removal (Eqs. (8) and (9)). In this case, H₂O₂ decomposition was faster, compared to the reaction employing pristine mesoporous TiO₂, which evidences that CWPO reactions account for the disappearance of the antibiotic species during the first 30 min of reaction (Fig. 4).

Table 2
Short chain acids detected at the end of reaction.

Catalyst and oxidant	Short-chain acids (mg·L⁻¹)		
	Oxalic	Acetic	Formic
TiO₂ + O₂	1.50	0.90	1.10
TiO₂ + H₂O₂	2.10	1.80	1.70
Fe₂O₃-TiO₂ + O₂	0.80	1.60	0.90
Fe₂O₃-TiO₂ + H₂O₂	0.02	0.05	0.03
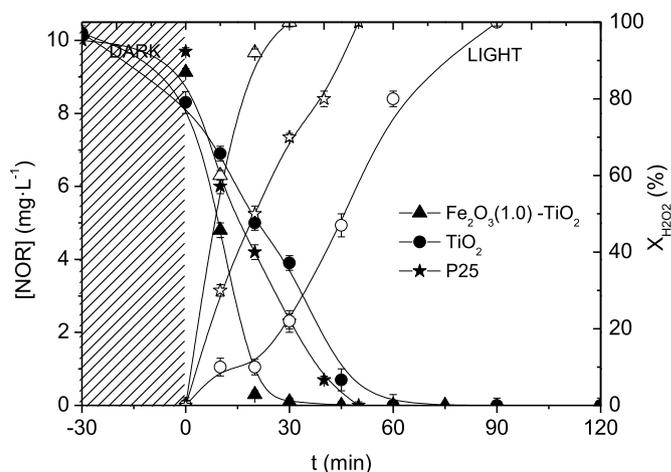
Fig. 4. Transient concentrations of norfloxacin (closed symbols) and H₂O₂ conversion (opened symbols) in aqueous solution during photo-oxidation at 298 K and pH 7 in the presence of P25, mesoporous TO₂, and mesoporous Fe₂O₃-TiO₂ (1 wt%) catalysts and under UV light illumination by a Hg lamp. (Operating conditions: [NOR] = 10 mg L⁻¹; [H₂O₂] = 26 mg L⁻¹; λ = 200–600 nm; V_R = 0.7 L).

$$Fe(II)-TiO_2 + H_2O_2 \rightarrow Fe(III)-TiO_2 + HO\cdot + OH^- \tag{8}$$

$$Fe(III)-TiO_2 + H_2O_2 \rightarrow Fe(II)-TiO_2 + HOO\cdot + H^+ \tag{9}$$
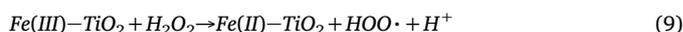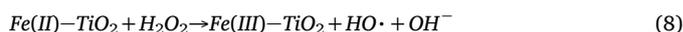
Moreover, the appearance of short-chain acids (Table 2) corroborates the overall degree of TOC conversion. Whereas mesoporous TiO₂ yielded larger concentrations of short-chain acid species, the mesoporous Fe₂O₃-TiO₂ catalysts produced almost none. It is reported that the formation of iron complexes with oxalic acid leads to the ligand-charge-metal transition (LCMT) mechanism, which promotes greater rates of mineralization and an iron regeneration, with the subsequent reduction of the leaching of active phase too (Pliego et al., 2016).

3.3. Irradiation influence

As shown above, the use of H₂O₂ as additional oxidant species improves the activity of the photocatalysts. Greater production of HO_x species is consistent with the faster observed removal of norfloxacin. H₂O₂-assisted reactions were conducted under UV–visible illumination with different distributions of wavelengths, specifically at 200–600 nm versus at 405 nm (with different instrumentation, as mentioned in the experimental part), both of which resulted in comparable degradation of the NOR species. This suggests that, so long as the photons penetrate into the reaction solution, the same or comparable degradation of the target compound could be obtained. Fig. 5 displays for each catalyst the same trends at the different instrumentation wavelengths. Interestingly, the oxidation rate and the light harvesting were enhanced for the mesoporous Fe₂O₃-TiO₂ catalyst for both UV–Vis wavelength distributions. This confirms that discrete 405 nm LED light is suitable for photoactivation of these materials.

Comparing the NOR decomposition activities of the different TiO₂ photocatalysts in Fig. 5, a reduction of the energy needed for a complete H₂O₂ depletion was seen when the 405 nm LED was used, specifically 2700 J m⁻² versus 2200 J m⁻², corresponding to less energy-intensive degradation of NOR. This suggests the improved efficacy of TiO₂ photocatalyst performances under LED light. As can be seen in Fig. 5, norfloxacin disappeared at a faster rate in the presence of mesoporous Fe₂O₃-TiO₂, than with mesoporous TiO₂, consistent with the increased production of oxidizing species by those reactions related to CWPO and the influence of light on the iron redox cycle (Eqs. (8) and (9)). It is noteworthy that the presence of iron not only promoted the decomposition of H₂O₂ at 900 J m⁻² (from a Hg lamp) and at 600 J m⁻² (from
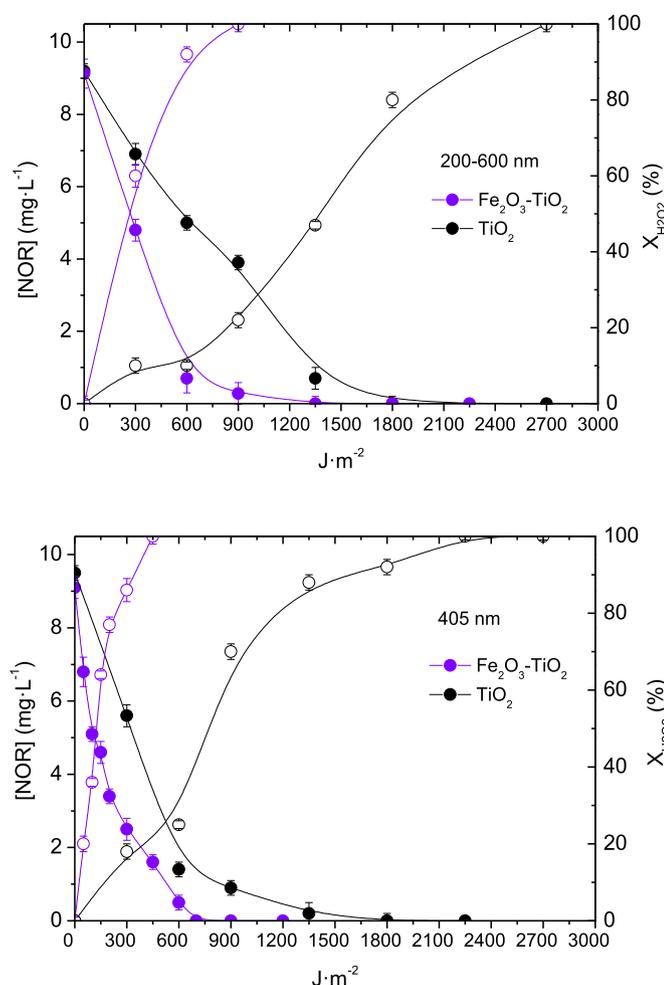
Fig. 5. Final concentrations of norfloxacin (closed circles) and H_2O_2 conversion (open circles) in aqueous solutions following photo-oxidation at 298 K and pH 7 in the presence of P25, mesoporous TO_2, and mesoporous Fe_2O_3-TiO_2 (1 wt%) catalysts and under UV light illumination at (A) 200–600 nm using a medium pressure Hg lamp or (B) at 405 nm using a LED. (Operating conditions: [NOR] = 10 mg L^{-1}; [H_2O_2] = 26 mg L^{-1}).

a LED), but also resulted in essentially complete antibiotic decomposition with a considerable reduction in the amount of energy required. Additionally, the short-chain acids detected were similar in both cases, which indicates analogous mechanistic pathways take place.

3.4. Iron load and catalyst stability

The above results provide evidence of the importance of surface iron species in photo-oxidation reactions. To assess the dependence of norfloxacin degradation on Fe-loading, the different Fe-containing mesoporous TiO_2 materials (Table 1) were compared as photocatalysts for NOR degradation (Fig. 6). Fe_2O_3(1.0)-, Fe_2O_3(1.5)-, Fe_2O_3(2.1)- and Fe_2O_3(3.0)-TiO_2 catalysts all decomposed H_2O_2 within the first 20 min of reaction (Fig. 6A), with higher surface Fe contents resulting in higher NOR decomposition rates, as manifested by the transient concentrations of H_2O_2. This is related to reactions of iron with H_2O_2, as indicated in Eqs (8) and (9).

A similar trend was observed for the transient concentrations of NOR (Fig. 6B), which suggests that H_2O_2 depletion occurs mainly through the formation of hydroxyl radicals. This is consistent with the formation of large amounts of short-chain acids for the TiO_2 catalysts containing more iron. The grafting of iron onto titania also led to a reduction in the time needed for NOR elimination, specifically from
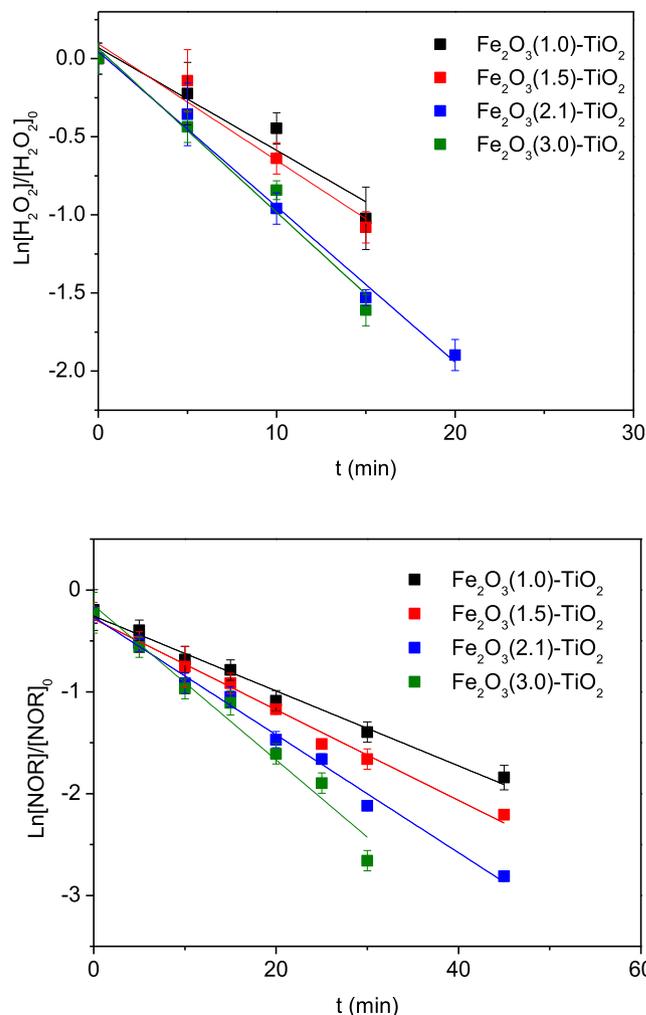
Fig. 6. Linear regression of (A) H_2O_2 consumption and (B) norfloxacin degradation in aqueous solution for different Fe_2O_3-TiO_2 catalysts under UV illumination at 405 nm using LED light under identical conditions at 298 K and pH 7. (Operating conditions: [NOR] = 10 mg L^{-1}; [H_2O_2] = 26 mg L^{-1}; λ_{LED} = 405; V_R = 0.1 L). Lines represent models of best fits for a pseudo-first-order reaction.

45 min to 30 min (Fig. 6B). TOC reduction exceeded 90% for all of the catalysts, so that secondary reactions can be dismissed.

The transient concentrations of H_2O_2 and norfloxacin during UV illumination at 405 nm in the presence of the different mesoporous Fe_2O_3-TiO_2 photocatalysts were modelled for a pseudo-first-order reaction. The rate constants obtained for mesoporous Fe_2O_3(1.0)-, Fe_2O_3(1.5)-, Fe_2O_3(2.1)-and Fe_2O_3(3.0)-TiO_2 for H_2O_2 consumption were 0.066, 0.075, 0.099 and 0.105 min^{-1}, respectively. For NOR degradation, rate constants were determined to be 0.037, 0.045, 0.058 and 0.076 min^{-1}, respectively, manifesting the higher reactivities of catalysts with higher surface Fe contents (Table 3). These results clearly indicate the direct relation between surface iron content and rate of NOR decomposition, which appears also to be related to the CWPO reactions (Eqs. (8) and (9)).

Nevertheless, the increase of k'_{H2O2} with the iron percentage was not linear. The values reached a plateau-curve for the higher concentrations indicating that greater doses of iron will not increase the rate associated to the CWPO contribution (Supplementary Information, Fig. S7).

While the activity for norfloxacin decomposition is improved, the stability of supported iron catalysts is still an issue to consider. Table 4 shows the leached iron concentration after reaction under the

Table 3
Fe-loading dependence of pseudo kinetic rate constants for H_2O_2 and NOR degradation from aqueous solutions at 298 K and pH 7 over mesoporous Fe_2O_3-TiO_2 photocatalysts.

Catalyst	k'_{NOR} (min^{-1})/R^2	k'_{H2O2} (min^{-1})/R^2
Fe_2O_3 (1.0)-TiO_2	0.037/0.99	0.066/0.98
Fe_2O_3 (1.5)-TiO_2	0.045/0.99	0.075/0.99
Fe_2O_3 (2.1)-TiO_2	0.058/0.99	0.099/0.97
Fe_2O_3 (3.0)-TiO_2	0.076/0.98	0.105/0.99

Table 4
Leached iron concentrations from the different mesoporous Fe_2O_3-TiO_2 photocatalysts after norfloxacin degradation from aqueous solutions at 298 K and pH 7.

Catalyst	$[Fe]_{leached}$ (mg·L^{-1})
Fe_2O_3 (1.0)-TiO_2	0.02
Fe_2O_3 (1.5)-TiO_2	0.04
Fe_2O_3 (2.1)-TiO_2	0.03
Fe_2O_3 (3.0)-TiO_2	0.02
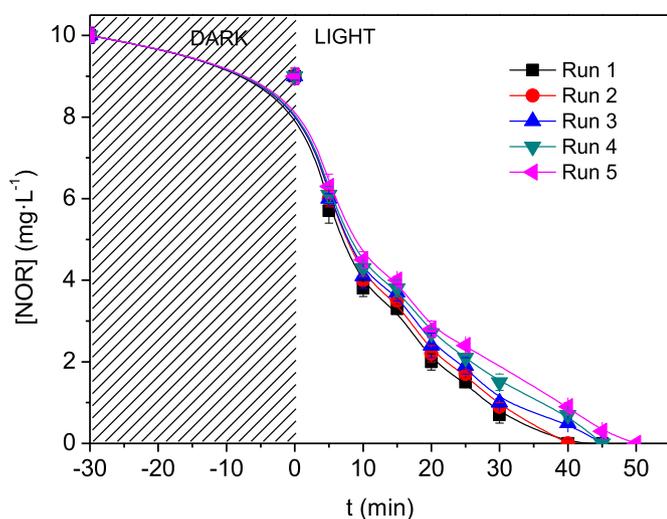
Fig. 7. Norfloxacin degradation in the presence of mesoporous Fe_2O_3 (3.0)-TiO_2 catalysts over several sequential runs using Fe_2O_3(3.0)-TiO_2 catalyst at 298 K and pH 7. (Operating conditions: [NOR] = 10 mg L^{-1}; [H_2O_2] = 26 mg L^{-1}; λ_{LED} = 405; V_R = 0.1 L). Lines have been added as guides for the eye.

conditions described above (298 K, pH 7). As can be seen, leached iron concentrations were very small and appear to be independent of the amount grafted onto the mesoporous Fe_2O_3-TiO_2 surfaces. Leached iron concentrations were less than 0.1% of the total amount of surface iron present in all cases. This overcomes one of the main previous drawbacks of this type of catalyst for which more severe leaching of iron has been reported (Munoz et al., 2013; Zazo et al., 2006).

To get insight into catalyst stability, several sequential cycles of the reused catalyst were performed for the most active mesoporous Fe_2O_3(3.0)-TiO_2 sample. After each run, the catalyst was recovered by filtration and dried at 60 °C overnight. Fig. 7 shows plots of norfloxacin concentration in aqueous solution under identical reaction conditions (298 K, pH 7) as a function of time for 5 reaction cycles. In all cases, essentially complete antibiotic removal was obtained, with only a slight kinetic difference between runs 1 and 5, which corroborates the high activities and stabilities of these mesoporous Fe_2O_3-TiO_2 catalysts. Thermogravimetric analyses (TGA) performed after each run (Supplementary Information, Fig. S4) showed negligible mass losses over the broad temperature range 20–1000 °C, which confirms the high

stabilities of the reused catalysts and the scarce presence of adsorbed organics after reaction that could cause catalyst deactivation.

4. Conclusions

Mesoporous Fe_2O_3-TiO_2 catalysts have been shown to be active and stable for the photocatalytic oxidation of norfloxacin in aqueous solutions under mild reaction conditions at 298 K and pH 7. Whereas mesoporous TiO_2 without Fe showed comparable activity to that of the commercial P25 catalyst, the incorporation of iron significantly improved the activity of mesoporous Fe_2O_3-TiO_2 photocatalysts. The addition of H_2O_2 resulted in the generation of additional oxidative species which reduced the required time for norfloxacin oxidation. The best result was obtained with the catalysts containing a 3% (w/w) of surface Fe_2O_3 where the decomposition of H_2O_2 contributed to the maximum norfloxacin depletion rate. In addition, Fe_2O_3-TiO_2 improved the process efficacy by using 405 nm LED light. This composite of iron and titanium oxides allows taking advantage of the CWPO and photocatalysis processes in combination. The higher activity is the result of an broader absorbance spectrum and the generation of larger amounts of $HO_x·$ due to the contributions from additional reactions related to H_2O_2 depletion by iron. Essentially complete norfloxacin removal and almost a total mineralization were achieved within 120 min at 298 K and pH_0 = 7 under UV illumination at 405 nm and with a stoichiometric amount of H_2O_2. In addition, the low leached iron concentrations and high photocatalytic activities observed over five sequential runs established the high stability of mesoporous Fe_2O_3-TiO_2, making it promising as a photocatalyst for removal of norfloxacin or other antibiotics and related compounds from aqueous solutions.

Appendix A. Supplementary data

Supplementary data to this article can be found online at https://doi.org/10.1016/j.jenvman.2019.02.109.

References

Baquero, F., Martinez, J.L., Canton, R., 2008. Curr. Opin. Biotechnol. 19, 260.
Barbosa, M.O., Moreira, N.F.F., Ribeiro, A.R., Pereira, M.F.R., Silva, A.M.T., 2016. Water Res. 94, 257.
Bohdziewicz, J., Kudlek, E., Dudziak, M., 2016. Desalination Water Treat. 57, 1552.
Carraro, G., Barreca, D., Maccato, C., Bontempi, E., Depero, L.E., de Julián Fernández, C., Caneschi, A., 2013. CrystEngComm 15, 1039.
Chakraborty, S., Loutatidou, S., Palmisano, G., Kujawa, J., Mavukkandy, M.O., Al-Gharabli, S., Curcio, E., Arafat, H.A., 2017. J. Chem. Environ. Eng. 5, 5014.
Dinh, Q.T., Moreau-Guigon, E., Labadie, P., Alliot, F., Teil, M., Blanchard, M., Chevreuil, M., 2017. Chemosphere 168, 483.
Dodd, M.C., Shah, A.D., von Gunten, U., Huang, C., 2005. Environ. Sci. Technol. 39, 7065.
Eisenberg, G., 1943. Colorimetric Determination of Hydrogen Peroxide, 15th ed. Industrial & Engineering Chemistry Analytical.
Emmanuel, E., Perrodin, Y., Keck, G., Blanchard, J.-, Vermande, P., 2005. J. Hazard Mater. 117, 1.
Fresno, F., 2013. Green Energy Technol. 71, 311.

Fresno, F., Hernández-Alonso, M.D., Tudela, D., Coronado, J.M., Soria, J., 2008. Appl. Catal. B Environ. 84, 598.

García-Muñoz, P., Pliego, G., Zazo, J.A., Bahamonde, A., Casas, J.A., 2016. J. Chem. Environ. Eng. 4, 542.

García-Muñoz, P., Pliego, G., Zazo, J.A., Bahamonde, A., Casas, J.A., 2017a. Chemosphere 180, 523.

García-Muñoz, P., Pliego, G., Zazo, J.A., Barbero, B., Bahamonde, A., Casas, J.A., 2017b. Chem. Eng. J. 318, 89.

García-Muñoz, P., Pliego, G., Zazo, J.A., Casas, J.A., 2018. J. Chem. Environ. Eng. 6, 7312.

He, K., Hain, E., Timm, A., Tarnowski, M., Blaney, L., 2019. Sci. Total Environ. 650, 3101.

Hernández, F., Calisto-Ulloa, N., Gómez-Fuentes, C., Gómez, M., Ferrer, J., González-Rocha, G., Bello-Toledo, H., Botero-Coy, A.M., Boix, C., Ibáñez, M., Montory, M., 2019. J. Hazard Mater. 363, 447.

Hughes, S.R., Kay, P., Brown, L.E., 2013. Environ. Sci. Technol. 47, 661.

Ismail, A.A., Abdelfattah, I., Faisal, M., Helal, A., 2018. J. Hazard Mater. 342, 519.

Jiang, C., Ji, Y., Shi, Y., Chen, J., Cai, T., 2016. Water Res. 106, 507.

Kanakaraju, D., Motti, C.A., Glass, B.D., Oelgemöller, M., 2016. Environ. Sci. Pollut. Control Ser. 23, 17437.

Kanakaraju, D., Glass, B.D., Oelgemöller, M., 2018. J. Environ. Manag. 219, 189.

Korovin, E., Selishchev, D., Besov, A., Kozlov, D., 2015. Appl. Catal. B Environ. 163, 143.

Kundu, V.S., Chauhan, N., Kumar, S., 2017. Indian J. Pure Appl. Phys. 55, 881.

Lee, S.C., Lintang, H.O., Yuliati, L., 2017. Beilstein J. Nanotechnol. 8, 915.

Litter, M.I., Navío, J.A., 1996. J. Photochem. Photobiol., A 98, 171.

Liu, P., Zhang, H., Feng, Y., Yang, F., Zhang, J., 2014. Chem. Eng. J. 240, 211.

Liu, H., Zhang, Z.-, Wang, X.-, Nie, G.-, Zhang, J., Zhang, S.-, Cao, N., Yan, S.-, Long, Y.-, 2018. J. Phys. Chem. Solid. 121, 236.

Luan, P., Xie, M., Liu, D., Fu, X., Jing, L., 2014. Sci. Rep. 4, 6180.

Malato, S., Fernández-Ibáñez, P., Maldonado, M.I., Blanco, J., Gernjak, W., 2009. Catal. Today 147, 1.

Moniz, S.J.A., Shevlin, S.A., An, X., Guo, Z., Tang, J., 2014. Chem. Eur J. 20, 15571.

Munoz, M., de Pedro, Z.M., Menendez, N., Casas, J.A., Rodriguez, J.J., 2013. Appl. Catal.,
B: Environ 136–137, 218.

Měšťánková, H., Mailhot, G., Jirkovský, J., Krýsa, J., Bolte, M., 2005. Appl. Catal. B Environ. 57, 257.

Paíga, P., Correia, M., Fernandes, M.J., Silva, A., Carvalho, M., Vieira, J., Jorge, S., Silva, J.G., Freire, C., Delerue-Matos, C., 2019. Sci. Total Environ. 648, 582.

Pliego, G., Garcia-Munoz, P., Zazo, J.A., Casas, J.A., Rodriguez, J.J., 2016. Environ. Sci. Pollut. Res. 1.

Rey, A., García-Muñoz, P., Hernández-Alonso, M.D., Mena, E., García-Rodríguez, S., Beltrán, F.J., 2014. Appl. Catal. B Environ. 154–155, 274.

Sandell, E., 1945. Colorimetric determination of traces of metals. J. Phys. Chem. 49, 263–264.

Sarkar, S., Chakraborty, S., Bhattacharjee, C., 2015. Ecotoxicol. Environ. Saf. 121, 263.

Shao, P., Ren, Z., Tian, J., Gao, S., Luo, X., Shi, W., Yan, B., Li, J., Cui, F., 2017. Chem. Eng. J. 323, 64.

Shard, A.G., 2014. Surf. Interface Anal. 46, 175.

Tryba, B., Morawski, A.W., Inagaki, M., Toyoda, M., 2006. Appl. Catal. B Environ. 63, 215.

Van Doorslaer, X., Dewulf, J., Van Langenhove, H., Demeestere, K., 2014. Sci. Total Environ. 500–501, 250.

Verlicchi, P., Al Aukidy, M., Zambello, E., 2012. Sci. Total Environ. 429, 123.

Wang, X., Li, Y., Li, R., Yang, H., Zhou, B., Wang, X., Xie, Y., 2019. Chemosphere 215, 124.

Yalçın, Y., Kılıç, M., Çınar, Z., 2010. Appl. Catal. B Environ. 99, 469.

Yang, P., Zhao, D., Margolese, D.I., Chmelka, B.F., Stucky, G.D., 1999. Chem. Mater. 11, 2813.

Yu, S., Wang, Y., Sun, F., Wang, R., Zhou, Y., 2018. Chem. Eng. J. 337, 183.

Zazo, J.A., Casas, J.A., Mohedano, A.F., Rodríguez, J.J., 2006. Appl. Catal. B Environ. 65, 261.

Zazo, J.A., Pliego, G., García-Muñoz, P., Casas, J.A., Rodriguez, J.J., 2016. Appl. Catal. B Environ. 192, 350.

Zhu, J., Chen, F., Zhang, J., Chen, H., Anpo, M., 2006. J. Photochem. Photobiol. Chem. 180, 196.